

Superresolution Imaging Using a Tapered Bundle of High-Refractive-Index Optical Fibers

G.M. Katyba,^{1,2,*} M. Skorobogatiy,³ D.G. Melikyants,⁴ N.V. Chernomyrdin,¹ A.N. Perov,⁴ E.V. Yakovlev,⁴ I.N. Dolganova,² I.E. Spektor,¹ V.V. Tuchin^{5,6} V.N. Kurlov⁶ and K.I. Zaytsev^{1,4,†}

¹Prokhorov General Physics Institute of the Russian Academy of Sciences, Moscow, Russia

²Institute of Solid State Physics of the Russian Academy of Sciences, Moscow, Russia

³Department of Engineering Physics, Polytechnique Montreal, Montreal, Canada

⁴Bauman Moscow State Technical University, Moscow, Russia

⁵Saratov State University, Saratov, Russia

⁶Institute of Precision Mechanics and Control of the Russian Academy of Sciences, Federal Research Centre
“Saratov Scientific Centre”, Saratov, Russia



(Received 22 June 2022; revised 13 August 2022; accepted 16 August 2022; published 26 September 2022)

The spatial resolution of an optical fiber bundle is limited by the size of a mode propagating in an individual fiber, which can be as small as a single wavelength approximately λ for conventional low-to-medium refractive-index optical fibers. High-refractive-index optical fiber bundles have a potential for the subwavelength-resolution imaging due to strong mode confinement in a fiber core, but they suffer from inconvenient image readout from the bundle output end, which is done by energy-inefficient near-field probes. To address this issue, this work introduces a tapered high-refractive-index terahertz (THz) optical fiber bundle. It comprises the subwavelength-diameter sapphire optical fibers, that are stacked tightly in the object plane to sample the near field with a subwavelength resolution. The fibers diverge from the object plane and, thus, stretch the captured near field for its further read out from the output bundle end using conventional diffraction-limited lens. Such a tapered fiber bundle was investigated numerically and then implemented experimentally at 0.33 THz. The subwavelength resolution of this bundle was confirmed, and varies over its aperture and can be as high as 0.35λ . The developed imaging principle allows the $\simeq 0.5\lambda$ Abbe resolution limit of a free-space focusing to be overcome and almost any common diffraction-limited optics for the near-field applications to be adapted.

DOI: 10.1103/PhysRevApplied.18.034069

I. INTRODUCTION

Currently, fiber bundles play a role in medical imaging, nondestructive testing, embedded equipment, and exposure technologies in different spectral ranges [1–10]. Moreover, some naturally occurring objects, such as regular bundles of axons in the brain white matter, were found to manifest light-guiding abilities similar to those of the optical fiber bundles [11,12].

In a conventional optical fiber bundle, each fiber is designed to operate independently of others, with a negligible crosstalk between modes of adjacent fibers. The spatial resolution of a bundle is then defined by a fiber packing period p , that can be as small as the individual fiber diameter d . For common materials with low to moderate refractive index, the minimal bundle resolution can reach a

free-space wavelength approximately λ , while its further reduction is physically impossible due to challenges of modal confinement in a subwavelength fiber cores [13,14]. This is the reason why conventional optical fiber bundles are not used in superresolution imaging [15].

Recently, alternative modalities of computational imaging were reported, that use a single fiber in the highly multimoded regime as an alternative to the optical fiber bundles [16,17]. Although promising, such imaging systems require complicated data processing for the image reconstruction and are highly sensitive to the environmental variations and mechanical influences. Moreover, the resolution of such imaging modalities is still limited by the low refractive index of a fiber core.

Another way to achieve superresolution is by using a wire medium [18], where dielectric fibers are replaced with metal wires, that are stretched between the object and image planes, suspended in free space, and acting as independent plasmonic waveguides. Wire media has a potential

*katyba_gm@issp.ac.ru

†kirzay@gmail.com

for the advanced resolution down to approximately $10^{-1}\lambda$ thanks to the strong confinement of plasmonic modes [19–22]. Nevertheless, a free-standing wire medium is impractical in real-world applications, while it also suffers from strong interwire crosstalk when operating in subwavelength imaging regime. These difficulties can be partially mitigated by suspending metal wires in a dielectric media [23,24], however, this significantly increases absorption and dispersion of the plasmonic modes, thus negating key advantages of a wire medium. Finally, while wire media were experimentally realized in the MHz and THz ranges [25,26], their translation to the infrared and visible bands is a daunting task, due to both the technological complexity and lower conductivity of metals in these ranges [18].

Most recently, high-refractive-index optical fiber bundles were developed based on sapphire fibers to overcome the Abbe resolution limit in the THz range [14]. Such fibers combine unique physical properties of sapphire, such as high THz refractive index, small absorption coefficient, chemical inertness, mechanical and radiation strength, with technological advantages of the edge-defined film-fed growth (EFG) technique, that allows production of high-quality flexible fibers directly from the Al_2O_3 melt with no mechanical processing [27,28]. Theoretical and experimental studies of sapphire fiber bundles confirmed their imaging capabilities [14], with the resolution as small as 0.3λ . Despite the advanced resolution, the THz image readout from the output bundle facet was not trivial, which is in fact a general problem both for optical fiber bundles and wire media. Indeed, bundles (or wire media) transfer only THz near field from the object plane to the image plane, while a scanning-probe near-field imaging system is still required to read the image with subwavelength resolution. This considerably limits the practical utility of such optical fiber bundles and wire media.

To address this challenge, in this paper, a tapered all-dielectric fiber bundle, that comprises a divergent array of high-refractive-index optical fibers, is developed for the THz superresolution imaging (Fig. 1). The bundle is made of a 21×21 -square lattice of $300\text{-}\mu\text{m}$ -diameter sapphire optical fibers, that are suspended in epoxy resin and form individual pixels. Using numerical analysis, the bundle is judiciously designed to enable superresolution imaging at the frequency of $\nu = 0.33$ THz with minimal crosstalk between pixels. The fibers fit tightly in the object plane, and form close-to-square lattice, with the period of $p = 0.35$ mm and total side of a square $P = 7.0$ mm. The array then diverges, while preserving the square-lattice symmetry in its cross section. The bundle thickness is $\simeq 11.25$ mm, while the final lattice period is 3 times larger than that in the object plane. This leads to stretching of the near field by a magnification factor of $K \simeq 3$, which makes possible its readout from the output bundle facet by a conventional wide-aperture diffraction-limited lens.

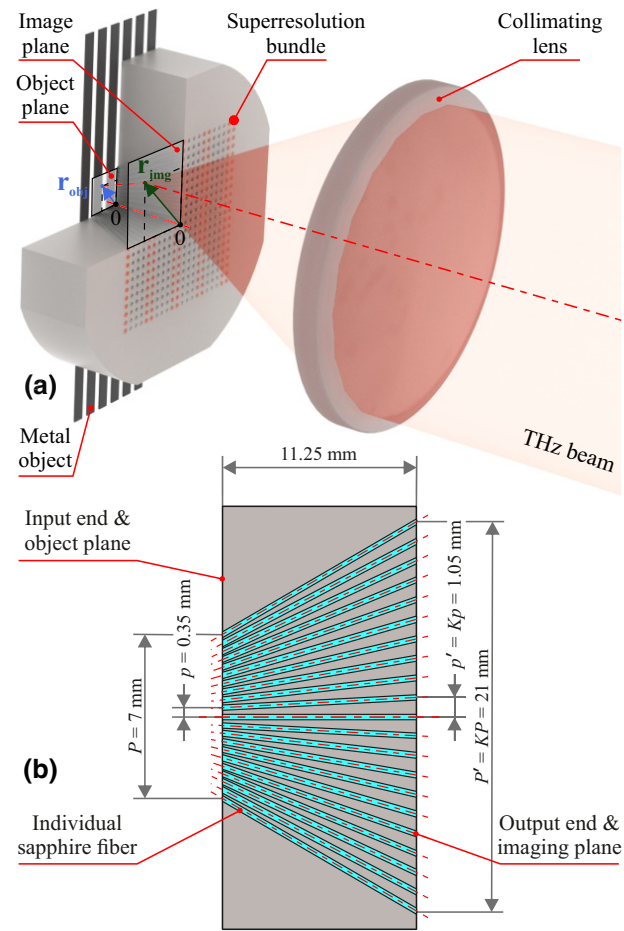


FIG. 1. (a) Schematic of the near-field imaging using a tapered bundle of high-refractive-index optical fibers, where the image is read out from the output bundle end using a conventional diffraction-limited optics. (b) Axial cross section of a tapered bundle with geometrical definitions.

Numerical and experimental studies demonstrate that this bundle can be applied to THz imaging with superresolution down to 0.35λ . It features high-energy efficiency due to the absence of any subwavelength apertures or probes in the readout optics. Moreover, such bundles can be interrogated directly with THz focal-plane arrays, thus enabling real-time superresolution imaging.

II. NUMERICAL ANALYSIS OF A TAPERED BUNDLE

To comprehensively analyze the spatial resolution of the tapered bundle, both the guiding properties of an individual fiber and the interfiber crosstalk effects in an array of diverging fibers should be taken into account.

First, we study modal properties of a simple step index fiber featuring sapphire core suspended in epoxy resin cladding, with the sapphire c axis directed along the fiber symmetry axis. By taking bulk THz optical properties of

sapphire from Ref. [14] (including anisotropy, materials' dispersion and absorption) and those of epoxy resin from Ref. [29], guiding properties of a 300- μm -diameter fiber are analyzed using the finite-difference eigenmode method (FDEM) of the ANSYS Mode software. In Fig. 2(a), we show the computed effective refractive index n_{eff} and propagation loss α (by power) for several lowest-order guided modes of a sapphire fiber.

From the figure it follows that our fiber operates in the effectively two-mode regime, as only the two lowest-order modes HE₁₁ and TE₀₁ have low enough losses α , to propagate through an approximately 1-cm-long bundle. Even for these modes losses increase greatly at lower frequencies ≤ 0.25 THz, due to weak confinement in the core and strong field overlap with high-loss cladding. Similarly, modal losses increase greatly at higher frequencies ≥ 0.5 THz, due to increasing THz-wave absorption by sapphire. Thus, the spectral range of effective THz guidance in an epoxy-cladded sapphire fiber is limited by $\simeq 0.25 - 0.5$ THz. While HE₁₁ and TE₀₁ modes have very different intensity distributions in the fiber core [Fig. 2(b)], both can be excited in the tapered bundle due to symmetry breaking in such structures.

In the absence of interfiber crosstalk, the resolution parameter δ can be defined analytically as a function of

the fiber diameter d and the free-space electromagnetic wavelength λ or frequency v :

$$\delta = \frac{d}{\lambda} = \frac{dv}{c_0}. \quad (1)$$

As shown by the blue line in Fig. 2(c), for a fixed diameter of an individual fiber d , this analytical resolution parameter δ increases linearly with frequency v . At smaller frequencies $v < 0.48$ THz, the analytical resolution overcomes the Abbe limit of a free-space focusing $\delta < 0.5$. To qualify the effect of a crosstalk, numerical modeling of a 9×9 diverging fiber array with the geometry equal to that from Fig. 1 is performed in the 0.2–0.5 THz range, using the finite-element frequency-domain (FEFD) method within the COMSOL Multiphysics software (see Appendix A). The results of these simulations are summarized in Figs. 2(c)–2(e). By exciting only the central pixel at the input bundle end, a frequency-dependent point-spread function (PSF) of a bundle is estimated [Fig. 2(e)]. The numerical resolution parameter δ is then calculated at different frequencies v by fitting this PSF with the Gaussian function, followed by estimation of its FWHM [Fig. 2(c)]. Thus calculated resolution δ is shown by green circles in Fig. 2(c). It has strong frequency-dependent character

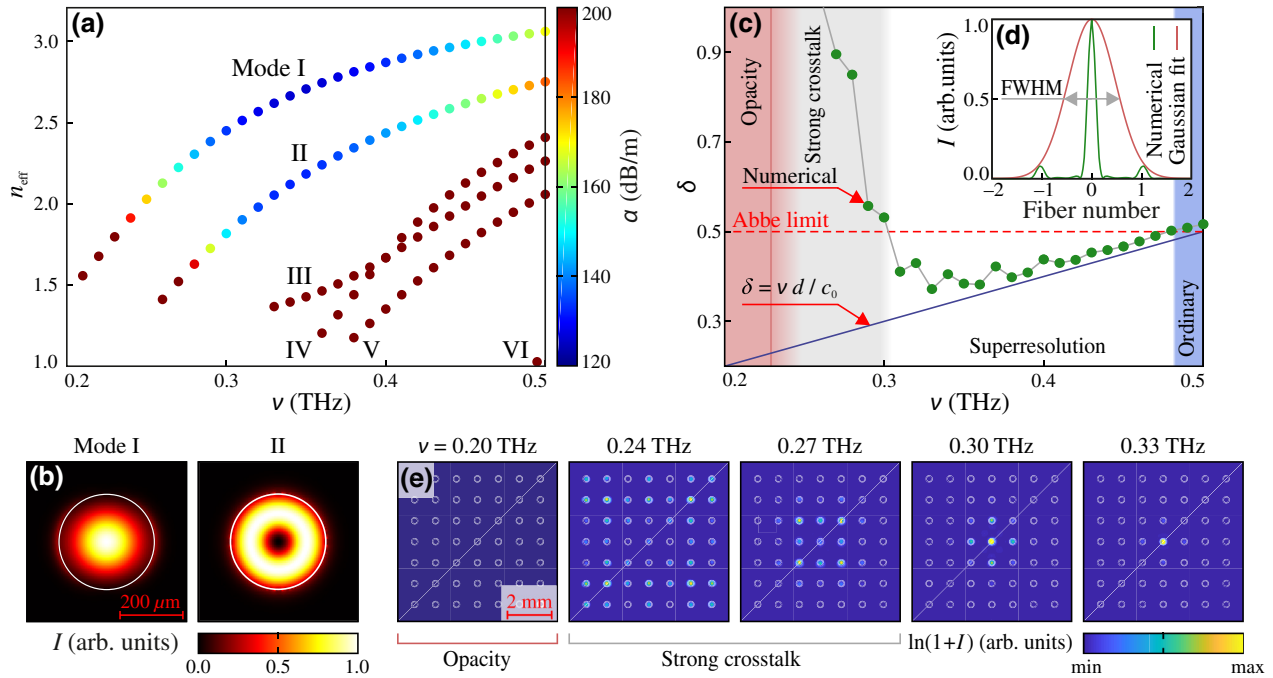


FIG. 2. Numerical modeling of the THz lightguiding in a tapered fiber bundle. (a) Effective refractive index n_{eff} and propagation loss α (by power) of several low-loss guided modes in a single 300- μm -diameter sapphire fiber cladded with an epoxy resin. (b) Intensity distributions $I \propto \mathbf{E}^2$ of the two lowest-loss modes I and II at 0.33 THz. (c) Analytical and FEFD numerical estimates of the resolution parameter δ . (d) FEFD estimates of the bundle PSF in the presence of crosstalk effect. (e) FEFD estimates of field intensities at the output bundle facet, when only the central fiber is excited at the input end. In (c), distinct regimes of a tapered bundle operation are labeled as opacity, strong crosstalk, superresolution, and ordinary.

due to the interfiber crosstalk. Numerical simulations allow identification of the following spectral regimes of a tapered bundle operation:

- (a) *Opacity*—at low frequencies $\nu \leq 0.24$ THz, the bundle is nontransparent.
- (b) *Strong crosstalk*—at $\nu \in (0.24, 0.3)$ THz, the resolution δ appears to be above the Abbe limit due to strong interfiber crosstalk.
- (c) *Superresolution*—at $\nu \in (0.3, 0.48)$ THz, the interfiber crosstalk can be largely neglected, while the resolution δ overcomes the Abbe limit.
- (d) *Ordinary*—at $\nu \geq 0.48$ THz, the bundle can still be used for imaging, but loses the superresolution capabilities.

Our numerical simulations predict the smallest value of the resolution parameter to be $\delta \simeq 0.35$ at the frequency of $\nu \simeq 0.33$ THz. This particular frequency is therefore selected for further experimental study of a tapered bundle.

III. FABRICATION OF A TAPERED BUNDLE

Sapphire fibers are fabricated using the EFG technique of shaped crystal growth directly from the Al_2O_3 melt [27, 28, 30, 31], which is detailed in Appendix B and in Ref. [32]. The as-grown fibers are then cut into $\simeq 2$ -cm-long pieces and only those with diameter d in the $300 \pm 20 \mu\text{m}$ range are retained. In Figs. 3(a) and 3(b), microscopy of a typical sapphire fiber end facet and a photo of a set of fibers, used in the fiber bundle assembly, are presented.

As shown in Figs. 3(c) and 3(d), a diverging fiber array is assembled using a porous polymer mold, which is fabricated using three-dimensional (3D) printing (Anycubic

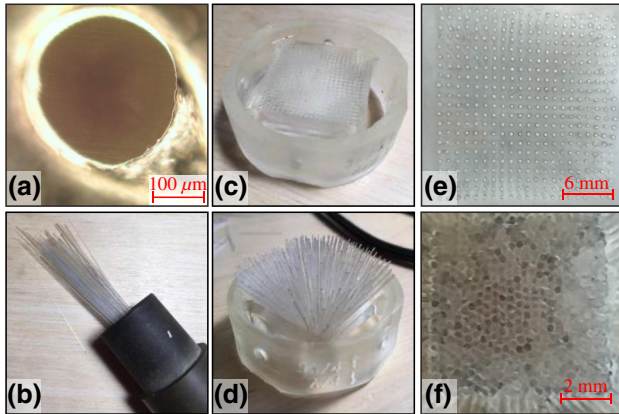


FIG. 3. Fabrication of a tapered fiber bundle. (a) Microscopy of the individual $\simeq 300\text{-}\mu\text{m}$ -diameter core of the EFG-grown sapphire fiber handled in free space. (b) Photo of the monodisperse ($d = 300 \pm 20 \mu\text{m}$) sapphire fibers prepared for the bundle assembly. (c),(d) 3D-printed polymer mold before and after insertion of sapphire fibers, respectively. (e),(f) Microscopy of the output and input ends, respectively, of the tapered bundle.

LCD Photon printer with the lateral and depth resolution of 47 and $30 \mu\text{m}$, correspondingly). The mold features an array of $\simeq 400\text{--}500\text{-}\mu\text{m}$ -diameter holes, into which the sapphire fibers are inserted. The mold with the fibers is then submerged into epoxy resin followed by curing. The input and output ends of a bundle are then defined by grinding and polishing of the cured monolith, which is illustrated in Figs. 3(e) and 3(f). As a result, at the output bundle facet (image plane), the fibers form an almost perfect square array [Figs. 3(e)] while at the input facet (object plane), the fiber array is somewhat disordered caused by small fiber displacement during epoxy curing [Figs. 3(f)]. Nevertheless, the fiber array remains regular by maintaining the same order at the input and output ends.

IV. EXPERIMENTAL STUDY OF A TAPERED BUNDLE

Imaging using a tapered fiber bundle is studied, using an in-house transmission-mode continuous-wave 0.33-THz imaging system detailed in Appendix C. It uses a backward-wave oscillator, as a THz emitter, and a Golay cell, as a THz-beam detector. As shown in Fig. 1(a), in the experimental setup, an imaged object is positioned at a small distance ($\ll \lambda$) in front of the bundle input facet and illuminated by a slightly focused spatially homogeneous THz beam. In the case of such a small distance between the object and the input bundle end, the geometrical shadow approximation is valid—i.e., the THz field distribution in the object plane is equal to that in the plane of the input bundle end. This allows us to treat the input bundle end as the object plane.

Illumination of a partially opaque object forms a spatial distribution of the field intensity at the object plane $I_{\text{obj}}(\mathbf{r}_{\text{obj}})$, where \mathbf{r}_{obj} is the vector in the object plane. The THz field is then coupled into the fiber bundle, guided to the bundle output facet and stretched by the magnification factor $K \simeq 3$ by the diverging fiber array. At the bundle output facet, the THz field intensity distribution is formed $I_{\text{img}}(\mathbf{r}_{\text{img}})$, where \mathbf{r}_{img} is a vector in the image plane, which in the absence of fiber crosstalk and intermodal interference is related to the intensity distribution in the object plane as

$$I_{\text{img}}(\mathbf{r}_{\text{img}}) = I_{\text{obj}}\left(\frac{\mathbf{r}_{\text{img}}}{K}\right). \quad (2)$$

The intensity distribution $I_{\text{img}}(\mathbf{r}_{\text{img}})$ is then read out from the bundle output facet using a diffraction-limited imaging system. This system used a two-dimensional (2D) motorized raster scanner, on which a wide aperture diffraction-limited lens and a Golay cell are mounted. The lens collimates the THz wave from a diffraction-limited area of the output facet and directs it towards the detector.

A. Image processing

In Figs. 4(a)–4(i), a photo of a metal-grid test object, with the period of 1.8 mm and the metal strip width of 0.9 mm, as well as its THz images, acquired via the tapered fiber bundle at $\nu = 0.33$ THz ($\lambda = 917 \mu\text{m}$), are shown. While several periods of a metal grid are clearly visible in a raw THz image [Fig. 4(b)], it has to be further enhanced to alleviate the impact of various artefacts that are common for the fiber-bundle imaging; among them, *image pixelization* (the THz image looks like a speckle pattern), *image intensity fluctuations* (transmission of individual fibers changes over the bundle aperture due to variation in their optical properties), *salt and pepper noise* (some pixels can be broken or, oppositely, provide much higher transmission than average).

To mitigate these difficulties, digital processing of the such fiber-bundle-based THz images is performed. First, image pixelization is suppressed [Fig. 4(c)] using a square moving-average (smoothing) filter $f(\mathbf{r}_{\text{img}})$ at the bundle output facet with the width and height equal to the fiber array period:

$$I_{\text{filt}}(\mathbf{r}_{\text{img}}) = I_{\text{img}}(\mathbf{r}_{\text{img}}) \otimes f(\mathbf{r}_{\text{img}}). \quad (3)$$

Second, the THz image is rescaled by the inverse magnification factor K^{-1} to retrieve it in the object plane followed by resampling [Fig. 4(d)]. Finally, an inverse filtering is used to correct for the image intensity heterogeneities. To this end, we acquire a reference image $I_{\text{img}}^{\text{ref}}(\mathbf{r})$, at the output facet of an empty tapered bundle, and then apply smoothing and resampling using the same parameters as for the

THz image of a sample [Figs. 4(e)–4(h)]. Then, the sampling image of an object is normalized by the reference one using the following regularization procedure:

$$I_{\text{norm}}(\mathbf{r}_{\text{obj}}) = \frac{I_{\text{filt}}(\mathbf{r}_{\text{obj}})}{I_{\text{filt}}^{\text{ref}}(\mathbf{r}_{\text{obj}}) + N}, \quad (4)$$

where $N \simeq 0.1$ denotes the noise level in our THz images $I_{\text{filt}}^{\text{ref}}(\mathbf{r}_{\text{obj}})$ [14]. This level is determined as a standard deviation of noise in the THz image formed by a bundle; the input end of which is blocked by an opaque shield.

Thus reconstructed THz image in the object plane $I_{\text{norm}}(\mathbf{r}_{\text{obj}})$ is shown in Fig. 4(i), with the effects of image pixelization, intensity inhomogeneities, and damaged pixels effectively mitigated by the image processing.

B. Resolution estimation

To experimentally estimate the spatial resolution of the tapered fiber bundle, a standard technique that involves imaging of test objects with abrupt changes in their THz transmission properties is used [14]. Particularly, a stripe of metal foil with a straight edge is used as an object. Since fibers in our bundle are packed in a square lattice, the resolution can be studied in several directions (horizontal, vertical, and diagonal) as shown in Figs. 5(a)–5(f). To estimate the resolution, the first derivative of the image intensity profile $dI_{\text{norm}}(r)/dr$ is calculated in the direction r , that is perpendicular to the imaged edge of a metal foil. As the function $dI_{\text{norm}}(r)/dr$ can be considered as an approximation of our imaging system PSF [33], the resolution parameter δ is calculated at each point along the metal foil

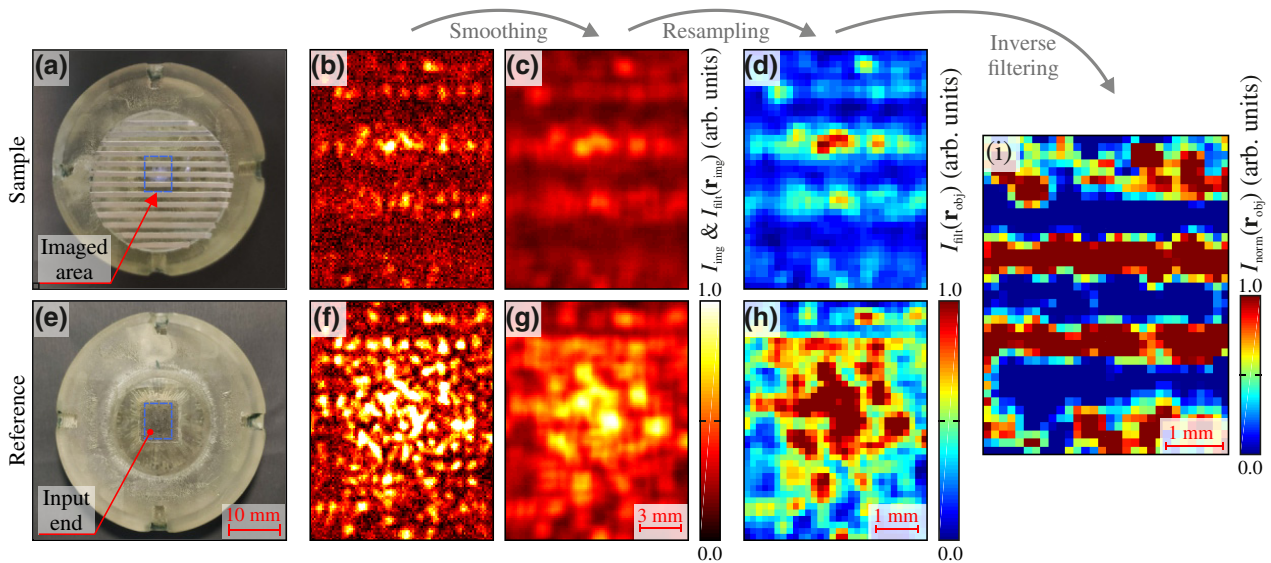


FIG. 4. Digital processing of the THz images acquired using the tapered fiber bundle at $\nu = 0.33$ THz ($\lambda \simeq 917 \mu\text{m}$). (a) Photo of the bundle input facet with a metal-grid object. (b) Measured $I_{\text{img}}(\mathbf{r}_{\text{img}})$, (c) smoothed $I_{\text{filt}}(\mathbf{r}_{\text{img}})$, and (d) rescaled and resampled $I_{\text{filt}}(\mathbf{r}_{\text{obj}})$ THz images of an object. (e) Photo of the empty bundle input facet (with no object) and corresponding reference THz images (f) $I_{\text{img}}^{\text{ref}}(\mathbf{r}_{\text{img}})$, (g) $I_{\text{filt}}^{\text{ref}}(\mathbf{r}_{\text{img}})$, and (h) $I_{\text{filt}}^{\text{ref}}(\mathbf{r}_{\text{obj}})$. (i) Normalized THz image $I_{\text{norm}}(\mathbf{r}_{\text{obj}})$ obtained via Eq. (4).

edge as the FWHM of the function central peak, normalized by $\lambda = 917 \mu\text{m}$. By examining different positions and orientations of the foil edge at the bundle input facet, statistics for the spatial distribution of the resolution parameter δ is collected and then fitted with the Gaussian function [Fig. 5(g)]. As expected, thus characterized resolution differs for the perpendicular and diagonal directions, with the mean values of $\langle \delta \rangle = 0.347$ and 0.543 and the standard deviations of $\sigma_{\delta} = 0.148$ and 0.171 , respectively, while always remaining strongly subwavelength.

The observed resolution variation over the bundle input facet can be rationalized by considering a disordered lattice formed by fibers in the object plane. Particularly, in Fig. 5(h), the photo of the bundle input facet is shown, while in Figs. 5(i) and 5(j), Voronoi cells and pair correlation function $g(r)$ are calculated for the corresponding partially disordered lattice formed by the sapphire fibers (nodes) [14]. In the Voronoi plot, the edge nodes (fibers) have a lower number of nearest neighbors, thus, complicating the data readability. Therefore, for convenience, in (i), we do not show cells for the edge nodes. From the Voronoi

plot in (i), one can notice that most nodes have six nearest neighbors, while this number fluctuates somewhat over the bundle aperture. While for the ideal crystalline lattice distinct peaks in a $g(r)$ function are the Dirac δ functions, for a somewhat disordered lattice, such peaks are broadened. Among them, the first and the second are notable, since they define statistics for the distances between a lattice node and its nearest neighbors in the vertical or horizontal and diagonal directions, correspondingly. By fitting the $g(r)$ -function peaks with the Gaussian function, the statistics for the nearest-neighbor separation [Fig. 5(j)] is found to be quite close to those from direct experimental resolution measurements [Fig. 5(g)]. Particularly, mean values $\langle \delta \rangle = 0.373$ and 0.515 for the first and second peaks almost perfectly agree with our experimental estimates, thus justifying the fiber lattice disordering as a main factor responsible for the resolution variation over the bundle aperture.

To summarize, the tapered fiber bundles, that use a diverged array of the high-refractive-index sapphire optical fibers, have been shown capable of superresolution

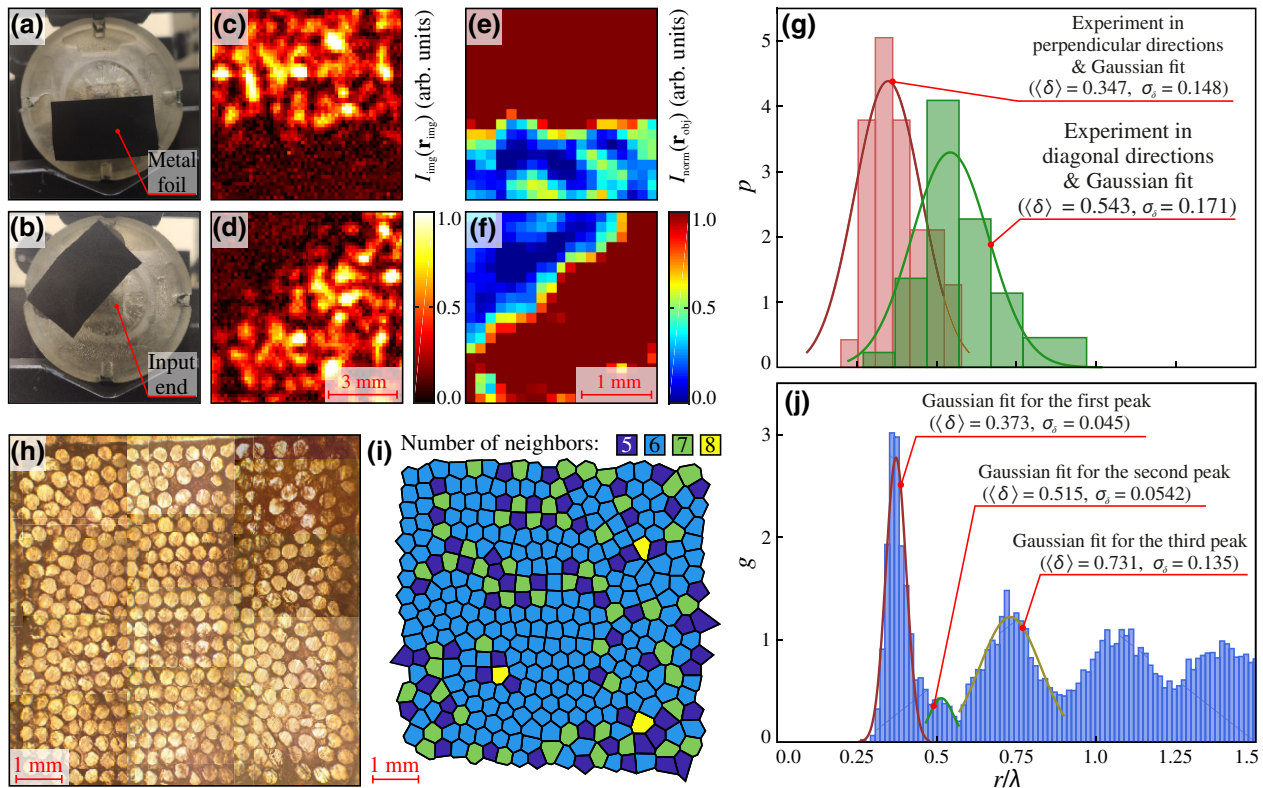


FIG. 5. Spatial resolution of the tapered fiber bundle at $\nu = 0.33 \text{ THz}$ ($\lambda \simeq 917 \mu\text{m}$). (a),(b) Photos of the metal stripe with a straight edge used as image objects orientated along horizontal, vertical, or diagonal directions. (c),(d) Measured $I_{\text{img}}(\mathbf{r}_{\text{img}})$ and (e),(f) normalized $I_{\text{norm}}(\mathbf{r}_{\text{obj}})$ THz images of this test object with distinct orientations. (g) Statistics of the resolution parameter δ variations over the bundle aperture for the perpendicular and diagonal directions, caused by the disordered fiber lattice and fitted by the Gaussian distribution. (h) Microscopy of the bundle input facet. (i) Representation of the bundle input facet using Voronoi cells, that are colored according to the number of nearest neighbors of each fiber (node). (g) A pair correlation function $g(r)$ for the partially disordered fiber lattice, along with the Gaussian fits for its first, second, and third peaks.

with the resolution parameter contrast $\delta = 0.347 \pm 0.148$ that matches well the numerically predicted value of $\delta = 0.35$, at the operation frequency $\nu = 0.33$ THz. Of note, such tapered fiber bundles allow convenient and energy-efficient readout using only standard diffraction-limited optical elements.

V. DISCUSSION

Despite the demonstrated potential of the tapered fiber bundles for superresolution imaging, further research is needed to boost the performance of this imaging modality, including the improvement of spatial resolution, energy efficiency, and image quality. Development of analytical and numerical models are also necessary to describe image formation in such diverging fiber bundles. Such models could also lead to development of the methods for resolving the inverse problems in imaging and reconstruction of various physical properties of an imaged object at the subwavelength scale [34].

Thanks to linearity of Maxwell's equations, the developed principles of the near-field imaging using the tapered high-refractive-index fiber bundles are general and can be translated to other spectral ranges. Therefore, tapered fiber bundles made from other high-refractive-index materials for operation in other-than THz spectral ranges can lead to alternative imaging applications. For example, in the infrared and visible ranges, one can use approximately 1- μm -diameter sapphire fiber grown by the micro pulling-down method [35] to assemble a high-refractive-index fiber bundle, or even resort to the rodlike oxide-oxide eutectic crystals grown by the EFG technique [36].

Finally, a problem of image readout from the bundle output facet still deserves additional research, as raster scanning with a single pixel detector is a slow process. The question of an optimal scanning step is still an open one. Eventually, one might also resort to using one- or two-dimensional detector arrays (such as arrays of the THz photoconductive antennas [37–39]), as they become more available. We notice that energy efficiency of such a superresolution imaging system can be further enhanced by using antireflection coatings of the input-output bundle ends [40], or even modern antireflection metasurfaces [41] to suppress Fresnel losses at these interfaces.

VI. CONCLUSION

In this work, the tapered bundles, comprising the divergent arrays of high-refractive-index optical fibers, are used in theoretical and experimental studies of superresolution imaging. Sapphire shaped crystals are used as a materials platform to fabricate a diverging bundle of optical fibers for the THz spectral range. Our findings reveal that such bundles can couple the THz near field at the object plane with the spatial resolution beyond the Abbe limit and then guide the thus captured near field from the object to the

image planes with low crosstalk. Along the way, the near field is spatially magnified due to the diverging geometry of the fiber array, which enables its readout from the bundle output facet using conventional diffraction-limited optics. Superior subwavelength resolution of the developed imaging modality is confirmed both numerically and experimentally to be 0.35λ .

ACKNOWLEDGMENTS

Fabrication of sapphire fibers by the EFG method, assembling of the fiber bundle, and numerical FDEM modeling of guiding properties of an individual sapphire fiber by G.M.K. were supported by the Russian Science Foundation (RSF), Project No. 22–72–10033. Experimental study of the THz imaging through a fiber bundle by N.V.C. and K.I.Z. are supported by the RSF Project No. 22–79–10099. Numerical FEFD modeling of the point-spread function of a tapered fiber bundle by M.S. is supported by the Ubiquitous Terahertz Photonics Project within the Canada Research Chairs Program.

APPENDIX A: NUMERICAL MODELING OF A TAPERED BUNDLE

The FEFD method within the COMSOL Multiphysics software is used to simulate transmission through diverging fiber bundles. A 3D computational cell includes a 9×9 diverging square array of circular fibers of diameter 0.3 mm and refractive index 3.067 [14]. The array is encased in epoxy resin with the refractive index of 1.59 and loss of 2 cm^{-1} (by field) [29]. It has the shape of a concatenated pyramid with the square bottom and top faces of sizes 3.15 and 9.45 mm, respectively, and height of 10 mm. The inclined fiber positions in the pyramid are chosen to reproduce the experimentally fabricated system (Fig. 3). On the top and on the bottom, the pyramid is padded with 1.2 mm of air followed by 1.2 mm of perfectly matched layer (PML). Above the pyramid smaller facet, a PML-backed interior port is used with the constant electric field directed along the x axis. To save computational resources, only a quarter of the pyramid is modeled with perfect electric conductor boundary conditions applied at the YOZ symmetry plane and the opposite (outer) side of the pyramid. Similarly, perfect magnetic conductor boundary conditions are applied at the XOZ symmetry plane and the corresponding opposite side of the pyramid. On the top and on the bottom, the PML regions are terminated with scattering boundary conditions. Maximal element size in a given domain is $\lambda / (5n)$, where n is the domain refractive index and λ is the free-space wavelength that in our simulations varies between $\lambda = 600 \mu\text{m}$ ($\nu \simeq 0.5$ THz) and 1.5 mm (0.2 THz). To the imaging system compute PSF, the top face of a prism is covered with a perfect electric conductor plate of thickness 50 μm featuring a square opening in the center of size 0.35 mm, with only one fiber core in the

center being open. Electric field distribution is recorded at the output face of the prism. Simulations are conducted on a double socket E5–2687W Xeon server with 512 GB of RAM using an out-of-core BiCGStab iterative solver with preconditioning. Maximal frequency is limited to 0.5 THz due to RAM overflow.

APPENDIX B: GROWTH OF SAPPHIRE FIBERS

Sapphire fibers are fabricated by the EFG technique in the ISSP RAS using the in-house experimental setup with high-frequency heating [27,28]. An automated system based on the *in situ* crystal weight sensor is used to obtain the sapphire fiber free of surface and bulk defects [30,31]. This setup allows production of sapphire-shaped crystals with complex predetermined cross-section geometries, high as-grown quality of the crystal surface and volume, aimed at solving the demanding problems in optics and photonics [27,28,32]. To grow 300- μm -diameter sapphire fibers with length of up to approximately 1 m, we apply the molybdenum crucible die, described in Ref. [14]. The main feature of this setup is a multirun growth regime, that is specially designed to fabricate simultaneously tens of sapphire fibers in a single growth cycle and, thus, to speed up the fiber bundle fabrication.

APPENDIX C: THZ-IMAGING SYSTEM

THz imaging through the tapered sapphire fiber bundles is performed in the GPI RAS using the in-house transmission-mode continuous-wave 0.33 THz ($\lambda \simeq 600 \mu\text{m}$) imaging system, which was applied in our earlier works on characterization of the metal-coated high-refractive-index sapphire fiber bundles [14]. As an emitter of continuous-wave THz radiation a backward-wave oscillator [42] was used, that was developed in GPI RAS and provides a linear polarization, tunable output frequency, the linewidth of approximately $10^{-5} \nu$, and the power of approximately 10^{-2} mW . As a detector of the modulated THz beam power flux, a Golay cell [43] was used, that was developed in GPI RAS and features the sensitivity of approximately 10^{-5} V/W , and the time response of approximately 10^{-1} sec . The THz beam is modulated at $\simeq 22 \text{ Hz}$ using a mechanical chopper and then detected via the demodulation of a signal from the Golay cell using a lock-in amplifier. A wide-aperture singlet (single lens) developed in Ref. [44] is used for the THz-image readout. The lens is made of the high density polyethylene, has two aspherical optical surfaces, as well as possesses the focal length of $f = 15 \text{ mm}$ and optical aperture of $D = 25.4 \text{ mm}$. Both the singlet and the Golay cell are mounted on a 2D motorized translation stage, which is used to raster scan the image plane with the positioning accuracy of $\leq 2 \mu\text{m}$ and the scanning step of $\leq 150 \mu\text{m}$ ($\simeq \lambda/6$), which satisfies the Nyquist-Shannon sampling theorem.

The object is rigidly fixed in front of the bundle by the small amount of plasticine in our experiments. However, other options are also available for the future work with such a tapered fiber bundle. For example, an imaged object can be handled in front of the input bundle end using a polymer holder, fabricated via modern 3D-printing technologies [45] and featuring the judiciously designed geometry, completely compatible with specific shape of the bundle.

- [1] Y. Lavi, A. Millo, and A. Katzir, Thin ordered bundles of infrared-transmitting silver halide fibers, *Appl. Phys. Lett.* **87**, 241122 (2005).
- [2] G. Keiser, F. Xiong, Y. Cui, and P. Shum, Review of diverse optical fibers used in biomedical research and clinical practice, *J. Biomed. Opt.* **19**, 080902 (2014).
- [3] L. Doronina-Amitonova, I. Fedotov, O. Efimova, M. Chernysheva, A. Fedotov, K. Anokhin, and A. Zheltikov, Multicolor *in vivo* brain imaging with a microscope-coupled fiber-bundle microprobe, *Appl. Phys. Lett.* **101**, 233702 (2012).
- [4] M. Krishnamurthi, E. Barnes, J. Sparks, R. He, N. Baril, P. Sazio, J. Badding, and V. Gopalan, A magnifying fiber element with an array of sub-wavelength Ge/ZnSe pixel waveguides for infrared imaging, *Appl. Phys. Lett.* **101**, 021108 (2012).
- [5] M. Pochechuev, I. Fedotov, and A. Zheltikov, An ultraslim all-fiber microendoscope for depth-resolved imaging, *Appl. Phys. Lett.* **113**, 191102 (2018).
- [6] J.-Y. Yu, S. Kim, Y. Shim, D. Holland, M. Allodi, C.-Y. Yeh, G. Blake, Y.-G. Han, and C.-L. Guo, Fiber-bundle illumination: Realizing high-degree time-multiplexed multifocal multiphoton microscopy with simplicity, *Sci. Rep.* **8**, 14863 (2018).
- [7] A. Orth, M. Ploschner, E. Wilson, I. Maksymov, and B. Gibson, Optical fiber bundles: Ultra-slim light field imaging probes, *Sci. Adv.* **5**, eaav1555 (2019).
- [8] V. Szabo, C. Ventalon, V. De Sars, J. Bradley, and V. Emiliani, Spatially selective holographic photoactivation and functional fluorescence imaging in freely behaving mice with a fiberscope, *Neuron* **84**, 1157 (2014).
- [9] A. Yetisen, H. Qu, A. Manbachi, H. Butt, M. Dokmei, J. Hinestroza, M. Skorobogatiy, A. Khademhosseini, and S. Yun, Nanotechnology in textiles, *ACS Nano* **10**, 3042 (2016).
- [10] L. Doronina-Amitonova, I. Fedotov, A. Fedotov, K. Anokhin, and A. Zheltikov, Neurophotonics: Optical methods to study and control the brain, *Physics-Uspekhi* **58**, 345 (2015).
- [11] S. Kumar, K. Boone, J. Tuszyński, P. Barclay, and C. Simon, Possible existence of optical communication channels in the brain, *Sci. Rep.* **6**, 36508 (2016).
- [12] D. Leykam and S. Flach, Perspective: Photonic flatbands, *APL Photonics* **3**, 070901 (2018).
- [13] D. Kim, J. Moon, M. Kim, T. Yang, J. Kim, E. Chung, and W. Choi, Toward a miniature endomicroscope: Pixelation-free and diffraction-limited imaging through a fiber bundle, *Opt. Lett.* **39**, 1921 (2014).

- [14] K. Zaytsev, G. Katyba, N. Chernomyrdin, I. Dolganova, A. Kucheryavenko, A. Rossolenko, V. Tuchin, V. Kurlov, and M. Skorobogatiy, Overcoming the Abbe diffraction limit using a bundle of metal-coated high-refractive-index sapphire optical fibers, *Adv. Opt. Mater.* **8**, 2000307 (2020).
- [15] R. Stantchev, B. Sun, S. Hornett, P. Hobson, G. Gibson, M. Padgett, and E. Hendry, Noninvasive, near-field terahertz imaging of hidden objects using a single-pixel detector, *Sci. Adv.* **2**, e1600190 (2016).
- [16] Y. Choi, C. Yoon, M. Kim, T. D. Yang, C. Fang-Yen, R. Dasari, K. Lee, and W. Choi, Scanner-Free and Wide-Field Endoscopic Imaging by Using a Single Multimode Optical Fiber, *Phys. Rev. Lett.* **109**, 203901 (2012).
- [17] N. Borhani, E. Kakkava, C. Moser, and D. Psaltis, Learning to see through multimode fibers, *Optica* **5**, 960 (2018).
- [18] C. Simovski, P. Belov, A. Atrashchenko, and Y. Kivshar, Wire metamaterials: Physics and applications, *Adv. Mater.* **24**, 4229 (2012).
- [19] P. Belov, C. Simovski, and P. Ikonen, Canalization of subwavelength images by electromagnetic crystals, *Phys. Rev. B* **71**, 193105 (2005).
- [20] P. Belov and M. Silveirinha, Resolution of subwavelength transmission devices formed by a wire medium, *Phys. Rev. E* **73**, 056607 (2006).
- [21] P. Belov, Y. Hao, and S. Sudhakaran, Subwavelength microwave imaging using an array of parallel conducting wires as a lens, *Phys. Rev. B* **73**, 033108 (2006).
- [22] M. Silveirinha, P. Belov, and C. Simovski, Subwavelength imaging at infrared frequencies using an array of metallic nanorods, *Phys. Rev. B* **75**, 035108 (2007).
- [23] A. Markov and M. Skorobogatiy, Hybrid plasmonic terahertz fibers for sensing applications, *Appl. Phys. Lett.* **103**, 181118 (2013).
- [24] M. Habib, A. Stefani, S. Atakaramians, S. Fleming, A. Argyros, and B. Kuhlmeier, A prism based magnifying hyperlens with broad-band imaging, *Appl. Phys. Lett.* **110**, 101106 (2017).
- [25] P. Belov, Y. Zhao, S. Sudhakaran, A. Alomainy, and Y. Hao, Experimental study of the subwavelength imaging by a wire medium slab, *Appl. Phys. Lett.* **89**, 262109 (2006).
- [26] K. Kaltenecker, A. Tuniz, S. Fleming, A. Argyros, B. Kuhlmeier, M. Walther, and B. Fischer, Ultrabroadband perfect imaging in terahertz wire media using single-cycle pulses, *Optica* **3**, 458 (2016).
- [27] G. Katyba, K. Zaytsev, I. Dolganova, I. Shikunova, N. Chernomyrdin, S. Yurchenko, G. Komandin, I. Reshetov, V. Nesvizhevsky, and V. Kurlov, Sapphire shaped crystals for waveguiding, sensing and exposure applications, *Prog. Cryst. Growth Charact. Mater.* **64**, 133 (2018).
- [28] G. Katyba, K. Zaytsev, I. Dolganova, N. Chernomyrdin, V. Ulitko, S. Rossolenko, I. Shikunova, and V. Kurlov, Sapphire waveguides and fibers for terahertz applications, *Prog. Cryst. Growth Charact. Mater.* **67**, 100523 (2021).
- [29] E. Yakovlev, K. Zaytsev, I. Dolganova, and S. Yurchenko, Non-destructive evaluation of polymer composite materials at the manufacturing stage using terahertz pulsed spectroscopy, *IEEE Trans. Terahertz Sci. Technol.* **5**, 810 (2015).
- [30] P. Antonov and V. Kurlov, A review of developments in shaped crystal growth of sapphire by the Stepanov and related techniques, *Prog. Cryst. Growth Charact. Mater.* **44**, 63 (2002).
- [31] N. Abrosimovi, V. Kurlov, and S. Rossolenko, Automated control of Czochralski and shaped crystal growth processes using weighing techniques, *Prog. Cryst. Growth Charact. Mater.* **46**, 1 (2003).
- [32] G. Katyba, K. Zaytsev, N. Chernomyrdin, I. Shikunova, G. Komandin, V. Anzin, S. Lebedev, I. Spektor, V. Karasik, S. Yurchenko, I. Reshetov, V. Kurlov, and M. Skorobogatiy, Sapphire photonic crystal waveguides for terahertz sensing in aggressive environments, *Adv. Opt. Mater.* **6**, 1800573 (2018).
- [33] D. F. Gardner, M. Tanksalvala, E. R. Shanblatt, X. Zhang, B. R. Galloway, C. L. Porter, R. Karl Jr., C. Bevis, D. E. Adams, H. C. Kapteyn, M. M. Murnane, and G. F. Mancini, Subwavelength coherent imaging of periodic samples using a 13.5 nm tabletop high-harmonic light source, *Nat. Photonics* **11**, 259 (2017).
- [34] N. Chernomyrdin, M. Skorobogatiy, A. Gavdush, G. Musina, G. Katyba, G. Komandin, A. Khorokhorov, I. Spektor, V. Tuchin, and K. Zaytsev, Quantitative super-resolution solid immersion microscopy via refractive index profile reconstruction, *Optica* **8**, 1471 (2021).
- [35] T. Fukuda, P. Rudolph, and S. Uda, *Fiber Crystal Growth from the Melt* (Springer, Berlin, 2004).
- [36] V. Kurlov, D. Stryukov, and I. Shikunova, Growth of sapphire and oxide eutectic fibers by the EFG technique, *J. Phys.: Conf. Ser.* **673**, 012017 (2016).
- [37] R. Henri, K. Nallappan, D. Ponomarev, H. Guerboukha, D. Lavrukhan, A. Yachmenev, R. Khabibullin, and M. Skorobogatiy, Fabrication and characterization of an 8×8 terahertz photoconductive antenna array for spatially resolved time domain spectroscopy and imaging applications, *IEEE Access* **9**, 117691 (2021).
- [38] S. Lepeshov, A. Gorodetsky, A. Krasnok, E. Rafailov, and P. Belov, Enhancement of terahertz photoconductive antenna operation by optical nanoantennas, *Laser Photonics Rev.* **11**, 1600199 (2017).
- [39] R. Leyman, A. Gorodetsky, N. Bazieva, G. Molis, A. Krotkus, E. Clarke, and E. Rafailov, Quantum dot materials for terahertz generation applications, *Laser Photonics Rev.* **10**, 772 (2016).
- [40] A. Gavdush, N. Chernomyrdin, Y. Lavrukhan, D. V. Cao, G. Komandin, I. Spektor, A. Perov, I. Dolganova, G. Katyba, V. Kurlov, M. Ponomarev, and D. S. Skorobogatiy, Proof of concept for continuously-tunable terahertz bandpass filter based on a gradient metal-hole array, *Opt. Express* **28**, 26228 (2020).
- [41] A. Bushunov, M. Tarabrin, and V. Lazarev, Review of surface modification technologies for mid-infrared antireflection microstructures fabrication, *Laser Photonics Rev.* **15**, 2000202 (2021).
- [42] G. A. Komandin, Sergey V. Chuchupal, S. P. Lebedev, Y. G. Goncharov, A. F. Korolev, O. E. Porodinkov, I. E. Spektor, and A. A. Volkov, BWO generators for terahertz dielectric measurements, *IEEE Trans. Terahertz Sci. Technol.* **3**, 440 (2013).

- [43] M. Golay, Theoretical consideration in heat and infrared detection, with particular reference to the pneumatic detector, *Rev. Sci. Instrum.* **18**, 347 (1947).
- [44] N. Chernomyrdin, M. Frolov, S. Lebedev, I. Reshetov, I. Spektor, V. Tolstoguzov, V. Karasik, A. Khorokhorov, K. Koshelev, A. Schadko, S. Yurchenko, and K. Zaytsev, Wide-aperture aspherical lens for high-resolution terahertz imaging, *Rev. Sci. Instrum.* **88**, 014703 (2017).
- [45] G. Xu, K. Nallappan, Y. Cao, and M. Skorobogatiy, Infinity additive manufacturing of continuous microstructured fiber links for THz communications, *Sci. Rep.* **12**, 4551 (2022).